Solar Energy Materials & Solar Cells 260 (2023) 112474

Contents lists available at ScienceDirect

Solar Energy Materials and Solar Cells

journal homepage: www.elsevier.com/locate/solmat

Directional oxygen diffusion in $Cu_{1.5}Mn_{1.5}O_4$ crystals for long reversible thermochemistry

Jiali Deng [a,b], Changdong Gu [c], Haoran Xu [a,b], Gang Xiao [a,b,*]

[a] Key Laboratory of Clean Energy and Carbon Neutrality of Zhejiang Province, Zhejiang University, Hangzhou, Zhejiang, 310027, China
[b] State Key Laboratory of Clean Energy Utilization, Zhejiang University, 38 Zheda Road, Hangzhou, 310027, China
[c] State Key Laboratory of Silicon Materials, College of Materials Science and Engineering, Zhejiang University, Hangzhou, Zhejiang, 310027, China

ARTICLE INFO

Keywords:
Solar energy
Thermochemical energy storage
Directional oxygen ion diffusion
Structure formation mechanism
Kirkendall effect
Long cycle life

ABSTRACT

Redox activity of metal oxides are the key to the development of high-temperature thermochemical energy storage. However, few studies have reported that the reactivity of metal oxides as thermochemical energy storage is significantly affected by the changes of crystal structure and morphology during redox, caused by ion diffusion and vacancy formation and migration. In this study, we find a previously unreported high-performance thermochemical energy storage material $Cu_{1.5}Mn_{1.5}O_4$ with special structure. $Cu_{1.5}Mn_{1.5}O_4$ shows high energy densities during reduction and oxidation (−219.852 and 207.618 kJ/kg), and keeps 97.06% and 92.98% reactivity after 600 cycles. Voids on specific surfaces are observed after cycling, but not in the fresh sample. We find the voids provide abundant Cu^{2+}, Mn^{4+} species and lattice oxygen to promote its reaction performance. Cu ions migrate obviously after oxidation and molecular dynamics simulations reveal that D_{Cu} (7.4×10^{-14} cm^2 s^{-1}) is higher than D_{Mn} (5.1×10^{-14} cm^2 s^{-1}) and D_O (1.7×10^{-14} cm^2 s^{-1}). $Cu_{1.5}Mn_{1.5}O_4$ exhibits voids during oxidation due to ion transport described by the Kirkendall effect. In addition, DFT calculations verify that O^{2-} is more easily to adsorb and diffuse on (111) surface, revealing the optimal transport path and directional diffusion mechanism of O^{2-}. These mechanisms can provide ideas for the reasonable design of materials to improve thermochemical reaction performance.

1. Introduction

As one of the most promising clean technologies in the renewable energy system, the Concentrating Solar Power (CSP) plays an increasingly important role [1,2]. CSP technology equipped with thermal energy storage (TES) can effectively solve the challenge of solar intermittency, shifting electricity production to the most valuable period to provide cost-effective and dispatchable renewable power [3,4]. Among them, thermochemical energy storage (TCES) is considered to be a better fit for the next generation CSP plants due to its advantages of operating at higher temperatures, higher energy density, unlimited transportation distance, and lower heat loss [4,5]. The metal oxide is the most potential candidate for TCES because of its better compatibility with CSP [6]. The metal oxide system based on solid-gas reversible reaction [7] completes the endothermic/exothermic reaction through the desorption/adsorption of oxygen on the material surface and the diffusion in the bulk. However, morphology greatly affects ionic diffusion, it is thus important to understand the morphological evolution of metal oxides during the redox for the design and development of materials with high performance [8].

Potential representatives of metal oxide systems for high-temperature thermochemical energy storage are Co_3O_4/CoO, Mn_2O_3/Mn_3O_4, CuO/Cu_2O, and their composites [9,10]. Pure metal oxides have been extensively studied their redox properties and enthalpy of reaction. It was found that Co_3O_4/CoO has good reactivity, but its toxicity and high cost limit the application [7,10–12]. Mn_2O_3/Mn_3O_4 re-oxidation kinetics is slow [10,13,14] and CuO/Cu_2O has serious sintering problems [10,15,16], resulting in poor reaction performance. But they are relatively cheap and have a wide range of resources. And their reaction performance can be improved by adjusting the reaction atmosphere or doping elements [17–23]. Researchers currently focus on the effect of doping modification on material properties and grain growth changes during cycles [18–25]. Liu et al. synthesized Co_3O_4 with different micro-nanostructured morphologies to evaluate their thermochemical energy storage performance [26]. However, the relationship between morphology evolution and ion diffusion during redox, the optimal

* Corresponding author. Key Laboratory of Clean Energy and Carbon Neutrality of Zhejiang Province, Zhejiang University, Hangzhou, Zhejiang, 310027, China.
E-mail address: xiaogangtianmen@zju.edu.cn (G. Xiao).

https://doi.org/10.1016/j.solmat.2023.112474
Received 5 April 2023; Received in revised form 24 June 2023; Accepted 18 July 2023
Available online 23 July 2023

transport path of oxygen ions and their related effect on the chemical properties and performances of materials have not been reported. It is worth noting that ion diffusion in metal oxides plays an important role during redox, accompanied by changes in morphology and structure [8]. Therefore, it is urgent to carry out research and in-depth understanding of these contents to clarify the nature of changes during the redox of metal oxides, thereby broadening the way of performance improvement. In addition, two researchers explored Cu–Mn mixed system for thermochemical energy storage, but both focused on the reactivity of $CuMn_2O_4$ spinel [27,28]. At present, the use of $Cu_{1.5}Mn_{1.5}O_4$ as a thermochemical energy storage material and the study of its reaction performance and evolution mechanism during redox have not been reported.

In this paper, we first discovered the thermochemical energy storage material $Cu_{1.5}Mn_{1.5}O_4$ with special structure and excellent performance. The changes of structure, morphology and surface chemical properties caused by the redox and their effects on the reactivity improvement were analyzed by experimental characterization. The nanostructure formation mechanism and directional oxygen diffusion mechanism in $Cu_{1.5}Mn_{1.5}O_4$ were further discussed by MD simulation and DFT calculation. This study can provide new insights for researchers in related fields to understand the ion and defect diffusion and morphological changes of metal oxides during redox, and guide the preparation and optimal design of thermochemical energy storage materials.

2. Experimental section

2.1. Material preparation

$Cu_{1.5}Mn_{1.5}O_4$ was synthesized by a simple sol-gel method. $Cu(NO_3)_2{\cdot}3H_2O$, $Mn(NO_3)_2$ with molar ratio of 1:1 were dissolved in appropriate amount of deionized water, and citric acid (metal ions:citric acid = 1:5) was added. The mixture was stirred at 70 °C for 3 h, and then ethylene glycol (citric acid: ethylene glycol = 3: 2) was added and stirred at 90 °C for 2 h. The gel was dried at 200 °C for 3 h and calcined at 450 °C and 900 °C for 4 h, respectively.

2.2. Material characterizations

The phase composition and crystal structures of the various samples at different stages were analyzed by powder X-ray diffraction (XRD). It was performed on an X'Pert Powder diffractometer equipped with Cu Kα radiation source (λ = 1.5406 Å) operating at 40 kV and 40 mA. The scanning rate was 0.02°, and the range of 2θ was 10–80°. The structural properties of the fresh sample was further identified by Fourier transform infrared (FTIR) spectra on a Thermo Scientific Nicolet iS20 spectrometer using KBr pellets in the range of 4000-400 cm^{-1} with a resolution of 4 cm^{-1}. The X-ray photoelectron spectroscopy (XPS) was used to obtain the information of surface chemistry of products. It was performed on a Thermo Scientific K-Alpha electron energy analyzer with monochromatic Al Kα (1486.6 eV) radiation, which was operated at 15 kV. The peak position of the element was calibrated using the binding energy (BE) of C1s at 284.8 eV. The simultaneous thermal analysis (TGA/DSC3+) was used for measuring the redox performance and energy storage/release density. The test conditions were air atmosphere with a flow rate of 50 mL/min, heating from 50 °C to 1100 °C for reduction and then cooling form 1100 °C–700 °C for oxidation at a heating/cooling rate of 20 °C/min. The micro-morphology, structure and element distribution of the samples were investigated by field emission scanning electron microscopy-energy-dispersive spectroscopy (FESEM-EDS) on a SU-8010 microscope equipped with an Oxford X-max80 spectrometer.

2.3. MD simulations

The molecular dynamics (MD) simulations were performed using a Large-scale Atomic/Molecular Massively Parallel Simulator (LAMMPS) [29]. To better describe the inter-atomic interaction of metal oxides, the Matsui-Akaogi (MA) potential was chosen [30]. The system was carried out in the canonical (NVT) ensemble. The simulation temperature and time step were set to 850 °C and 10 ps, respectively. To generate the O concentration gradient, we removed O atoms from the outermost layer.

2.4. DFT calculations

All spin-polarized density functional theory (DFT) calculations were carried out using the Vienna ab initio simulation program (VASP) [31]. The ionic cores were represented by using the projector augmented-wave (PAW) method potentials [32] with the following valence states: 3d10 and 4s1 for Cu, and 3d5 and 4s2 for Mn. Exchange and correlation functions are performed by generalized gradient approximation (GGA) based on functional Perdew-Burke-Ernzerhoff (PBE) approximation [33]. A Hubbard-like model of the GGA + U method [34] was applied to address the strong 3d electron correlations effect of Cu and Mn atoms. For the valence spectra of Mn 3d and Cu 3d levels, the U = 2.5 eV was selected accurately to describe the appropriate electronic structure and reaction energetics [35]. The plane wave cut-off energy was set to 450 eV. Spin polarized was used in all calculations. The (6 × 6 × 6) Monkhorst-Pack k-point grid was applied for the bulk calculations, while it was set at 4 × 4 × 1 for the surface calculations. For energy calculations, the electronic energy was converged to 1.0×10^{-5} eV, and convergence criterion for internal atomic coordinates until all forces were smaller than 0.025 eV/Å. The lattice constant of $Cu_{1.5}Mn_{1.5}O_4$ calculated by DFT was a = b = c = 8.363 Å, which was in good agreement with the experimental data (a = b = c = 8.303 Å) with small deviations (0.7%). The constructed surface slab model was further expanded into a p (2 × 2) unit cell, where the vacuum layer was set to 20 Å. The surface slab model consisted of 12 layers of atoms, with six fixed at the bottom and six relaxed at the top. For the energy barrier calculation of ion diffusion, the transition state was optimized by relaxing the force below 0.02 eV/Å using the climbing image nudged elastic band (CI-NEB) method [36].

3. Results and discussion

3.1. Structure characterization of prepared sample

The XRD analysis is performed to determine the crystal structure and phase composition of the prepared sample, and the results are shown in Fig. 1a. All intense diffraction peaks of the sample could be indexed as $Cu_{1.5}Mn_{1.5}O_4$ (ICDD-PDF No. 70–0260), which gave the 2θ values of 18.44°, 30.36°, 35.78°, 37.42°, 43.48°, 48.74°, 54.10°, 57.52°, 63.18° and 75.96°. They corresponded to the (111), (220), (311), (222), (400), (311), (422), (511), (440) and (533) crystal planes of the cubic spinel $Cu_{1.5}Mn_{1.5}O_4$. Furthermore, the diffraction peaks of the composite were intense, implying good crystallinity. As shown in Fig. 1e, Cu^+ occupies the A site (tetrahedron), while Cu^{2+} and Mn^{4+} occupy the B site (octahedron) in $Cu_{1.5}Mn_{1.5}O_4$ spinel crystal [37]. The Local enlargement FTIR spectra at the range of 1000-400 cm^{-1} have been presented in Fig. 1b. Characteristic bands of around 600 cm^{-1} and 500 cm^{-1} could be attributed to the lattice vibrations of Cu–O in tetrahedral sites (ν_A) and Mn–O in octahedral sites (ν_B) of spinel structure [38], respectively. The cation valence of the sample was identified by XPS. The Cu2p 3/2 spectra is shown in Fig. 1c, where 940–945 eV belongs to vibration satellite peaks [39]. The peak with binding energy at 930.7 eV corresponded to Cu^+, while the peak at 933.6 eV and satellite peaks belonged to Cu^{2+} [40]. Cu^+ species exists stably because of the interaction between Cu and Mn [41]. Fig. 1d presents the Mn 2p spectra, which there are two main peaks of Mn2p 1/2 and Mn2p 3/2, respectively. The binding energy of Mn 2p3/2 at 640.9 eV and Mn 2p1/2 at 652.6 eV were associated with Mn^{3+}, while the binding energy of Mn 2p3/2 at 642.5 eV and Mn 2p1/2 at 654.2 eV revealed the existence of Mn^{4+} cations [42,

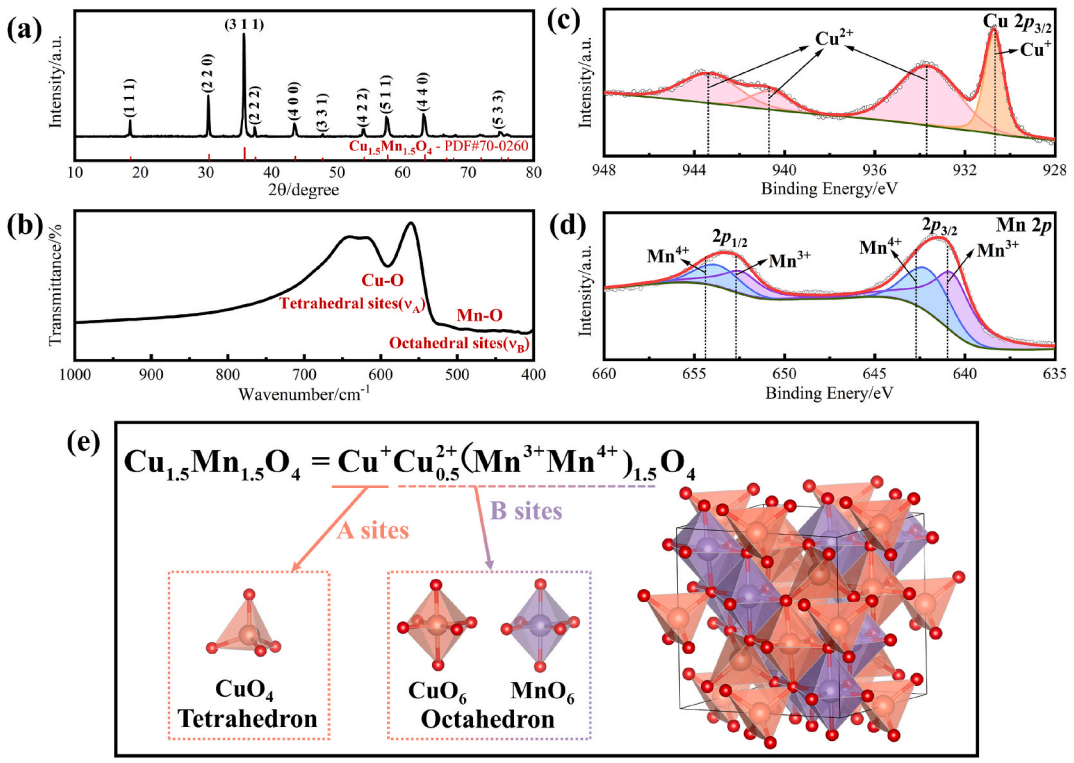

Fig. 1. Characterization of the crystal phase and chemical composition of the fresh sample. (a) XRD pattern. (b) Local enlargement FTIR spectra at the range of 1000-400 cm^{-1}. XPS spectra of (c) Cu 2p3/2 and (d) Mn 2p. (e) Schematic of the crystal structure.

43]. Accompanied by the loss of oxygen, part of Mn^{4+} ions are reduced to Mn^{3+} due to the charge neutrality [44]. Obviously, mixed Cu^{+}/Cu^{2+} and Mn^{3+}/Mn^{4+} were simultaneously presented in $Cu_{1.5}Mn_{1.5}O_4$ [45]. These results proved that the spinel $Cu_{1.5}Mn_{1.5}O_4$ had been successfully synthesized.

3.2. Reaction performance and cycle stability testing

The redox reactivity and cycle stability of $Cu_{1.5}Mn_{1.5}O_4$ is tested by TG/DSC, and the results are presented in Fig. 2. The results of the first cycle are shown in Fig. 2a, the reduction begin at 950 °C, and the peak

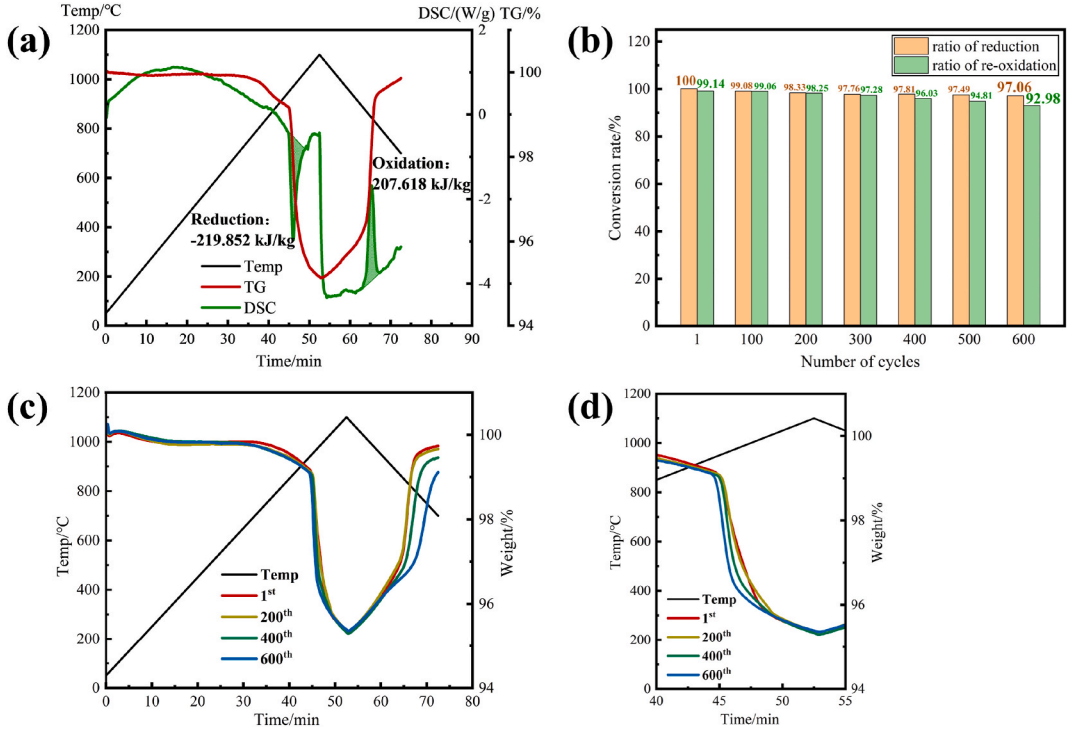

Fig. 2. The excellent performance of $Cu_{1.5}Mn_{1.5}O_4$. (a) First energy storage-release reactivity. (b) Reaction conversion rate during cycle. (c) TG curves at different cycles. (d) Partial TG curves of the reduction in different cycles.

temperature is 970 °C. The weight loss ratio during the reduction was 3.844%, and the thermochemical energy storage density reached −219.852 kJ/kg. The peak temperature during the oxidation was about 850 °C, and the weight gain ratio was 3.811%. The degree of re-oxidation achieved 99%. The energy release density was 207.618 kJ/kg, showing excellent chemical reversibility. Fig. 2b and c demonstrate that the reduction and oxidation conversion rates of $Cu_{1.5}Mn_{1.5}O_4$ keep 97.06% and 92.98% after 600 cycles, maintaining high reactivity. Based on the same application range, the results of comparing the reaction performance of Mn-based metal oxides are listed in Table 1. The above results showed that $Cu_{1.5}Mn_{1.5}O_4$ had high energy density and excellent cycle stability. It is worth noting that the slope of TG curve increases with the increase of the number of cycles during the reduction of $Cu_{1.5}Mn_{1.5}O_4$, indicating that the reduction rate is accelerating (Fig. 2d).

3.3. Evolution of structure and micromorphology during redox

The crystal structure transition process of $Cu_{1.5}Mn_{1.5}O_4$ during the redox was characterized by XRD. It is worth mentioning that after $Cu_{1.5}Mn_{1.5}O_4$ was reduced, we used nitrogen atmosphere to prevent it from being oxidized. As shown in Fig. 3a and b, the whole process is mainly composed of spinel $Cu_{1.5}Mn_{1.5}O_4$ (PDF#70–0262) and layered $CuMnO_2$ (PDF#50–0860). $Cu_{1.5}Mn_{1.5}O_4$ released oxygen and stored energy during the reduction, thus transforming into $CuMnO_2$. The oxidation process occurred reversible reaction, that is, $CuMnO_2$ completely transformed to $Cu_{1.5}Mn_{1.5}O_4$, which was consistent with the fresh sample. Therefore, the redox could be described by the following equation.

$$2Cu_{1.5}Mn_{1.5}O_4 \rightleftharpoons 3CuMnO_2 + O_2$$

Fig. 3c shows the morphology evolution of $Cu_{1.5}Mn_{1.5}O_4$ at different stages during redox. The prepared fresh sample presented regular polyhedral shape. However, the reduced $CuMnO_2$ particles had flake-like morphology of typical delafossite structural materials. Surprisingly, it could be clearly observed that $Cu_{1.5}Mn_{1.5}O_4$ had special void structure on some surfaces after a complete redox process. The structure was not observed in the fresh sample. It is speculated that the change may be due to the redox of the material, which is related to ions diffusion. In addition, the void structure formation increase the porosity of the material. The effective collision between reacting molecules in unit volume is increased, which is beneficial to promote the chemical reaction. Therefore, the $Cu_{1.5}Mn_{1.5}O_4$ with void structure exhibits a faster reduction rate in subsequent reduction cycles than the fresh samples, which explains the test results in Fig. 2d.

XPS was used to analyze the surface chemical properties of the materials after morphologic changes. The spectra of Cu 2p3/2 and Mn 2p are shown in Fig. 3d and e, respectively. After oxidation, the Cu^{2+} content of $Cu_{1.5}Mn_{1.5}O_4$ slightly increased from 73.63% to 80.83%, while the Mn^{4+} increased from 37.45% to 60.62%, indicating that the void structure formation promoted the oxidation of Cu^{+}/Cu^{2+} and Mn^{3+}/Mn^{4+}. Moreover, it is worth noting that it greatly increased the content of Mn^{4+}, resulting in more exposure of Mn^{4+} in the spinel octahedral position to the surface, and significantly, Mn^{4+} determined the reactivity [46]. Two typical peaks at 529.6 eV and 530.8 eV in Fig. 3f can be attributed to lattice oxygen and adsorbed oxygen [47]. It was observed that the lattice oxygen increased from 31.82% to 37.48% after oxidation. Adsorption and release of lattice oxygen is the rate-determining step in redox reaction [48]. Therefore, the increase of active lattice oxygen can improve the re-oxidation performance [25].

Table 1
Reduction and oxidation onset temperatures, energy density and cycle performance of Mn-based metal oxides in air.

Metal oxides	T_{red} (°C)	T_{ox} (°C)	Energy density (kJ/kg)	Cycle number
Mn_2O_3 [20]	940	~	−202 and ~	–
94% Mn_3O_4, 6% SiO_2 [18]	985	780	−180 and 117	9
95% Mn_2O_3+5% Cr [19]	972	785	−159.7 and ~	30
$(Mn_{0.8}Fe_{0.2})_2O_3$ [20]	978	878	−171.95 and 201.56	100
$CuMn_2O_4$+Mn_3O_4 [27]	968	915	~ and 14	5
$CuMn_2O_4$+CuO [28]	980	900	~ and 258.32 ± 15.31	20
$Cu_{1.5}Mn_{1.5}O_4$	950	890	−219.852 and 207.618	600

~ indicates that this parameter is not given in the reference.

3.4. Structural stability and formation mechanism

The voids evolution was further analyzed to reveal the structure formation mechanism and clarify its relationship with the reaction performance. As shown in Fig. 4a, not only the first redox occurs the structural transition (Fig. 3c), but the voids can still appear in multiple cycles. Moreover, the particle size increases rapidly with increasing cycle. This is due to the surface energy difference of different grain sizes driving the fusion of large grains and the merge of small grains into the large grains (Ostwald ripening) [49]. The crystal growth of $Cu_{1.5}Mn_{1.5}O_4$ conformed to the Kossel-Stranski model [50]. Under the actual growth conditions, the (111) crystal facet was assembled layer-by-layer resulting in the appearance of growth steps at the end. However, the void structure of $Cu_{1.5}Mn_{1.5}O_4$ on the specific surface could be clearly observed after different cycles, which was speculated to be related to the directional transport of oxygen ions. It was worth noting that the particles agglomerated and grew after multiple cycles, the large-sized particles still maintained this structure. It indicates that the voids keep stability, so the material has excellent cyclic reactivity (Fig. 2b and c). However, due to the sintering caused by repeated cycles at high temperature, the particle growth reduced the chemical reaction area, resulting in a slight decrease in the performance of $Cu_{1.5}Mn_{1.5}O_4$.

The redox processes are accompanied by the exchange of ions and electrons. These processes lead to the generation and diffusion of defects, which determine the crystal phase and morphology of the material and its subsequent chemical behavior. EDS mapping is used to analyze the surface of voids (Fig. 4b and S1). It was found that the Mn in $Cu_{1.5}Mn_{1.5}O_4$ was uniformly distributed, but Cu was enriched on the outer surface of the voids, indicating that the obvious migration of Cu cations occurred during the oxidation.

The ions diffusion of $Cu_{1.5}Mn_{1.5}O_4$ during the oxidation was simulated by MD. The nanoparticle model is constructed in three-dimensional space as shown in Fig. S2. To simulate the process of O atom transfer from $Cu_{1.5}Mn_{1.5}O_4$ to $CuMnO_2$, we artificially removed O atom form the outermost layer of $Cu_{1.5}Mn_{1.5}O_4$. The diffusion coefficient D of different atoms of $Cu_{1.5}Mn_{1.5}O_4$ at 850 °C was obtained by analyzing the mean square displacement (MSD) with the least square method based on Einstein relation. The MSD was calculated as:

$$\mathrm{MSD} \equiv <\Delta\vec{r}(t)^2> \equiv \frac{1}{N}\sum_{i=1}^{N}(\vec{r_i}(t) - \vec{r_i}(0))^2$$

MSD is proportional to the observation time t which tends to be infinity. The diffusion coefficient D was acquired by:

$$D \equiv \frac{1}{6}\lim_{t\to\infty}\frac{<[r(t_0+t) - r(t_o)]^2>}{t}$$

Here, $r_i(t)$ is the position of the atom at time t; N is the total number in the supercell; and the symbol $< >$ indicate an ensemble average has been taken. The ensemble average is an average over all atoms.

By recording the position of the atom as a function of time, we calculated the MSD. The model after atom diffusion at oxidation temperature (850 °C) and the MSD curves over time are shown in Fig. 4c and d, respectively. The MSD-Time curves had great linear relations after

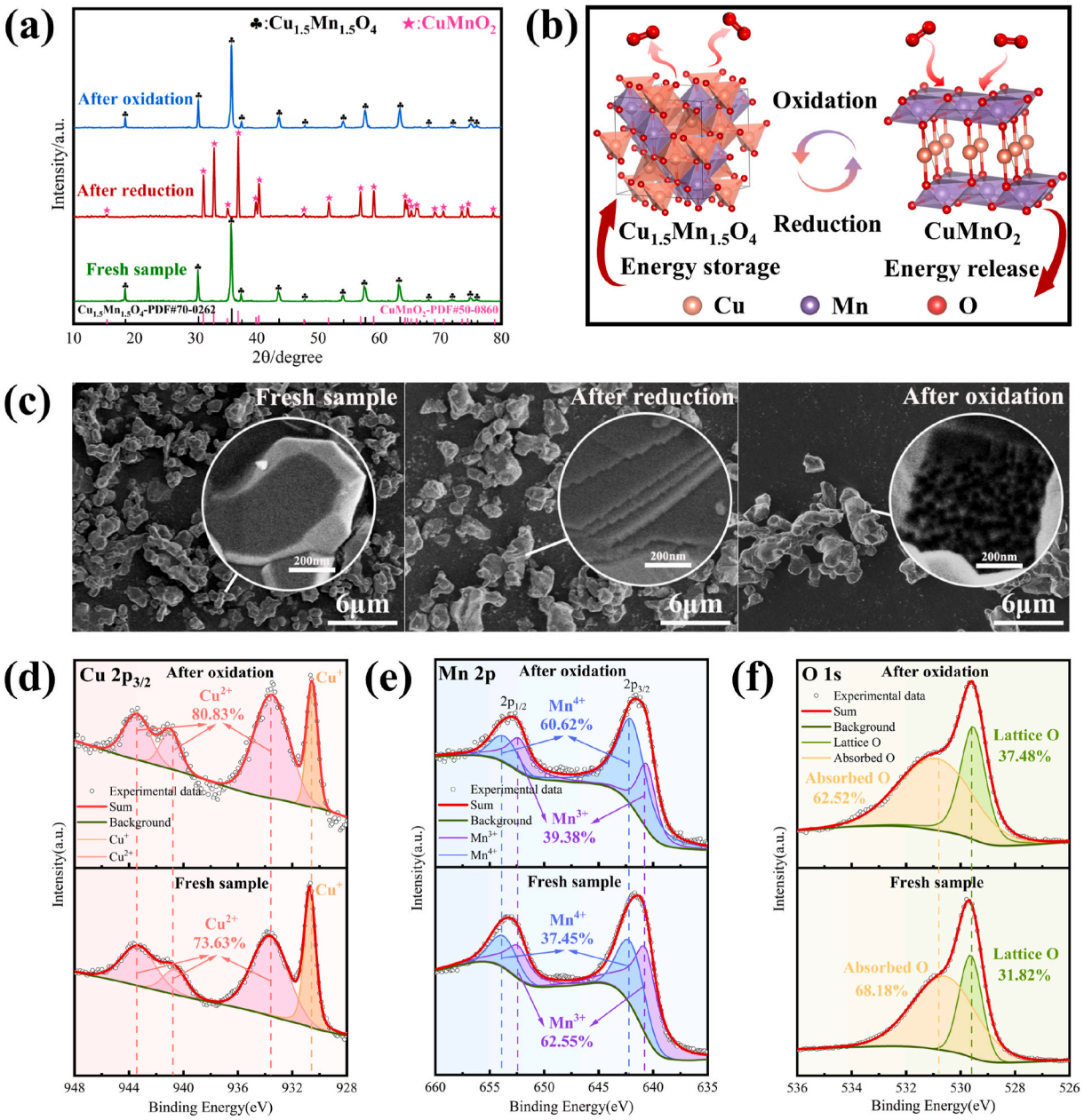

Fig. 3. Evolution of the structure and micromorphology during redox. (a) XRD patterns. (b) Schematic of phase transition. (c) FESEM images of the samples at different stages. XPS (d) Cu 2p3/2, (e) Mn 2p, and (f) O 1s of fresh and oxidized samples.

100 ps, and D was calculated by fitting the slope. D_{Cu} (7.4×10^{-14} cm^2 s^{-1}) was higher than D_{Mn} (5.1×10^{-14} cm^2 s^{-1}) and D_O (1.7×10^{-14} cm^2 s^{-1}), which was consistent with the experimental observation (Fig. 4b and S1).

This phenomenon can be attributed to the Kirkendall effect [51] (Fig. 4e). When the surface of $CuMnO_2$ was gradually oxidized to $Cu_{1.5}Mn_{1.5}O_4$, ions diffused along the crystal facet (111) perpendicular to the $Cu_{1.5}Mn_{1.5}O_4$ product layer, providing O^{2-} for the internal unreacted $CuMnO_2$ until the oxidation was complete. However, the outward diffusion of Cu and Mn cations was faster than the inward diffusion of O anions through vacancy-assisted exchange. Accordingly, the resulting unequal diffusion was balanced by oppositely diffused vacancies, which could condense into voids at dislocations. Therefore, voids on the specific surface of $Cu_{1.5}Mn_{1.5}O_4$ appeared. In addition, the surface aggregation of Cu cations is speculated to be due to the fact that Cu ions on the surface are more likely to react with O (vs. Mn ions), resulting in the concentration gradient of Cu ions in $Cu_{1.5}Mn_{1.5}O_4$. And the volume expansion of oxidation creates the physical space for ion diffusion, so that Cu ions transport outward faster. The particular structure can be described by the complex interaction of oxidation process, ion diffusion kinetics and mechanical expansion.

It is difficult to detect the effect of $Cu_{1.5}Mn_{1.5}O_4$ (111) surface termination on structure formation and ion diffusion by experimental characterization. However, one of the main mechanisms controlling structure formation and evolution is surface energy and diffusion in solid [52]. The minimum surface energy is the driving force for structure formation, and the diffusion determines the structure evolution. Therefore, the slab model optimization of different terminations on (111) surface of $Cu_{1.5}Mn_{1.5}O_4$ was further explored by DFT calculation. The results in Fig. 5a show that the Cu termination has the lowest surface energy of 1.194 J/m^2, compared to the Mn termination (including a small amount of Cu). It indicated that it was the most stable surface structure of $Cu_{1.5}Mn_{1.5}O_4$. The surface composed of Cu termination is easily exposed to the environment, so O anions are more easily bonded

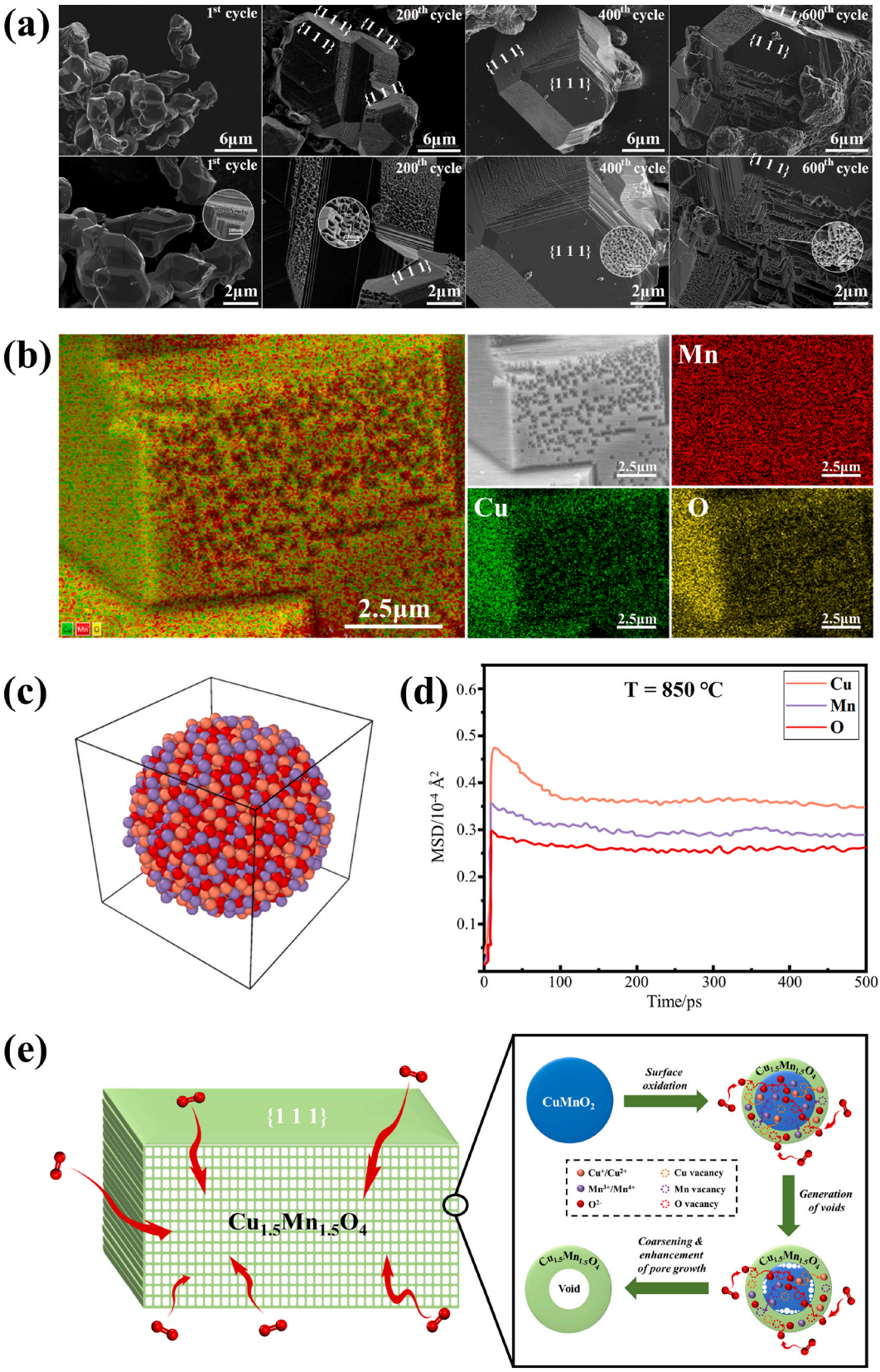

Fig. 4. The cyclic structural stability and formation mechanism of $Cu_{1.5}Mn_{1.5}O_4$. (a) FESEM images of the samples at different cycles. (b) SEM images and corresponding EDS mapping of $Cu_{1.5}Mn_{1.5}O_4$ on directional void surface. (c) Model after atomic diffusion. (d) Mean square displacements (MSD) of different atoms in $Cu_{1.5}Mn_{1.5}O_4$ versus time at 850 °C (Oxidation peak temperature). (e) Schematic of detailed formation mechanism of nanovoids by Kirkendall effect during the oxidation.

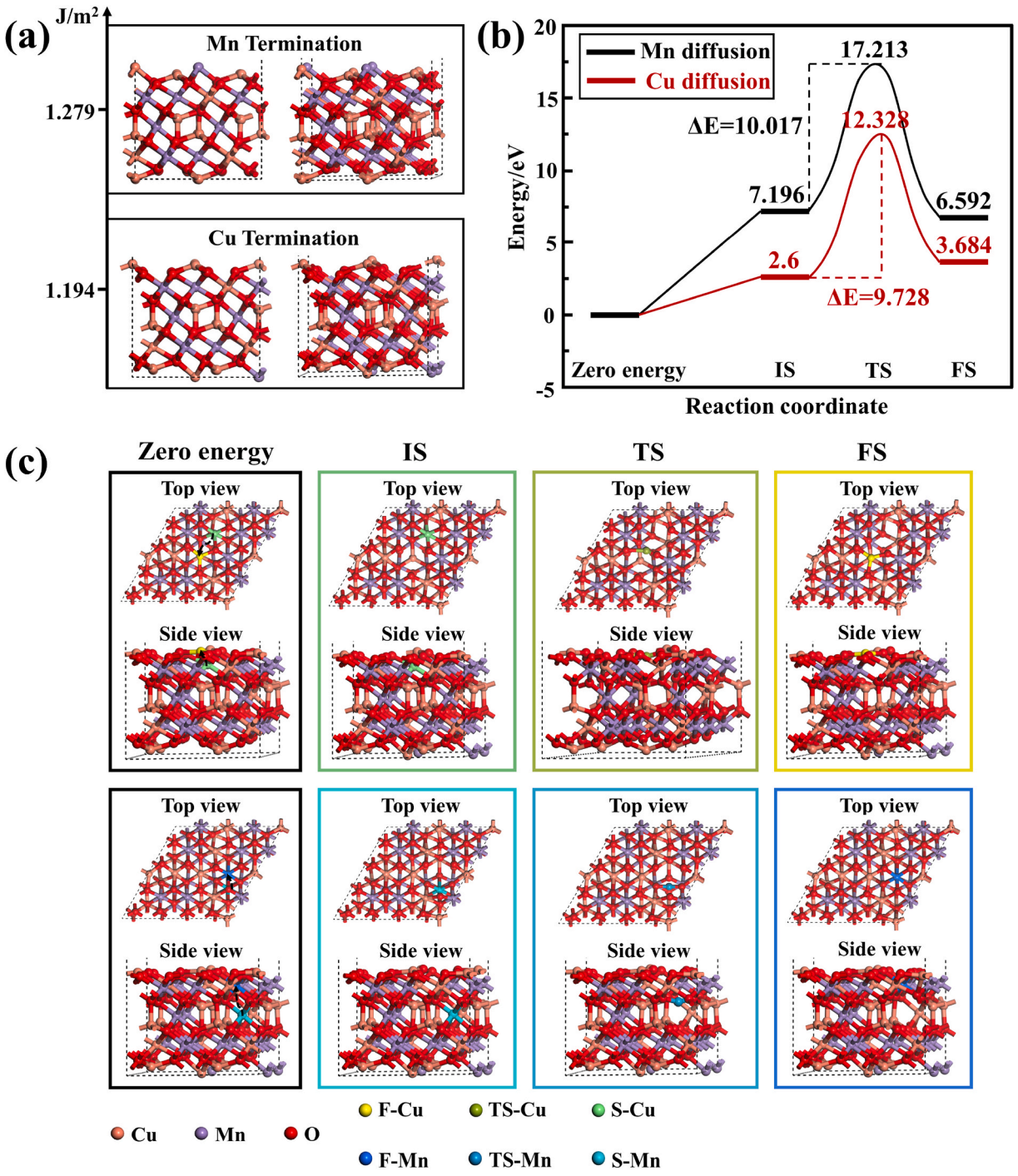

Fig. 5. Computation of surface structure growth and cation diffusion of $Cu_{1.5}Mn_{1.5}O_4$ by DFT. (a) Comparison of surface energy (E_{Surf}) of different terminals on (111) surface. (b) Vacancy formation energies and diffusion energy barriers (ΔE) of Cu and Mn cations. (c) Cu and Mn diffusion pathways on (111) surface of $Cu_{1.5}Mn_{1.5}O_4$. The zero energy corresponds to the complete slab model without vacancy. IS, TS and FS refer to the initial, transition and final states, respectively. The ions in the first atomic layer are labeled with "F" and in the second atomic layer with "S".

with Cu cations, which is consistent with the results in Fig. 4b and S1. In addition, the vacancy formation energies of Cu and Mn at different sites of $Cu_{1.5}Mn_{1.5}O_4$ are shown in Figs. S3 and S4. Thus, the outward transport pathways of Cu and Mn cations are determined and the diffusion energy barrier (ΔE) is calculated, as shown in Fig. 5b and c. The vacancy formation energy ($E(V_{Mn})$ = 7.196 eV and 6.592 eV) in different layers and the diffusion energy barrier (ΔE = 10.017 eV) of Mn were higher than those of Cu ($E(V_{Cu})$ = 2.6 eV and 3.684 eV, ΔE = 9.728 eV). It shows that Cu cations are easier to diffuse than Mn cations, which results are in agreement with Fig. 4d, which helps to explain the aggregation of Cu on the surface (Fig. 4b and S1).

3.5. Oxygen ion directional transport mechanism

Fig. 4a shows that $Cu_{1.5}Mn_{1.5}O_4$ only generates the void structure on the specific surface, so the directional oxygen ion transport mechanism of $Cu_{1.5}Mn_{1.5}O_4$ is further verified by DFT calculation. Low-index surfaces are easily exposed to the environment, so (100) and (110) are selected for comparison with (111). The surface energy (E_{Surf}) of different terminals of (100) and (110) are shown in Figs. S5 and S6. The

optimized structure with the lowest surface energy was used for calculation.

The oxygen vacancy formation energies at different positions on different surfaces are appeared in Figs. S7–S9. O^{2-} diffuses into the interior through oxygen vacancies. Fig. 6a and S10 demonstrate the adsorption energies and models on (100), (110) and (111) surfaces. The adsorption energy on (100) surface was 0.225eV, indicating that the adsorption process was endothermic and unstable. However, O^{2-} had the strongest adsorption capacity (−0.446 eV) and the most stable structure on (111) surface, elucidating that O^{2-} preferentially adsorbed on the (111) surface. The oxygen diffusion paths and calculation results on different surfaces are shown in Fig. 6b and c and S11–S13, respectively. Compared with (100) (2.349 eV) and (110) (2.083 eV), the oxygen vacancy formation energy $E(V_O)$ in the outermost layer of (111) was the lowest (0.512 eV). It indicated that the (111) surface promoted the formation of surface oxygen vacancies, providing active sites for surface reactions. In addition, the $E(V_O)$ in the bulk (1.765 eV) and oxygen migration energy barrier ΔE (4.5 eV) of (111) were lower than those of (100) ($E(V_O)$ = 2.309 eV, ΔE = 6.667 eV) and (110) ($E(V_O)$ = 1.811 eV, ΔE = 4.989 eV), elucidating that the oxygen vacancies inside the crystal also were also easier to generate and were conducive to improving oxygen ion diffusion kinetics. When the gas-solid reaction enters the diffusion stage through product layer, the diffusion of ions through the solid product becomes the main limiting factor of the reaction [53]. Therefore, the diffusion of O^{2-} in $Cu_{1.5}Mn_{1.5}O_4$ determined the redox reactivity. These results showed that the formation of oxygen vacancies through the inward diffusion of oxygen ions was easier on (111) than other surfaces during the reaction to form the porous surface, which explained the experiments. Therefore, the (111) surface of $Cu_{1.5}Mn_{1.5}O_4$ was the optimal transport path of oxygen ions during redox. Combined with the difference in ion diffusion rate, the directional voids was created, which was conducive to improving the reactivity and accelerating the reaction kinetics.

4. Conclusion

In summary, we have successfully prepared $Cu_{1.5}Mn_{1.5}O_4$ with spinel structure containing Cu^+/Cu^{2+} and Mn^{3+}/Mn^{4+} mixed valence states. It had high energy storage and release density (−219.852 kJ/kg and 207.618 kJ/kg) and excellent chemical reversibility. And the reduction and oxidation conversion rates kept 97.06% and 92.98% of the initial capacity after 600 cycles, respectively. The experiment found that the spinel $Cu_{1.5}Mn_{1.5}O_4$ and layered $CuMnO_2$ undergo reversible phase transitions during redox. Surprisingly, $Cu_{1.5}Mn_{1.5}O_4$ appeared the special void structure after one cycle, but not in the fresh sample. The nanostructure effectively increased the chemical reaction area and provided abundant Cu^{2+} and Mn^{4+} species and lattice oxygen for $Cu_{1.5}Mn_{1.5}O_4$, which was beneficial to promote the redox reactivity. Further structural evolution analysis showed that Cu ions migrated significantly. And the D_{Cu} was higher than D_{Mn} and D_O by MD simulation. The structure formation mechanism was related to the Kirkendall effect. DFT calculations was used to further verify the aggregation of Cu element on the surface and void formation mechanism. In addition, $Cu_{1.5}Mn_{1.5}O_4$ was observed to have voids on specific surfaces. DFT

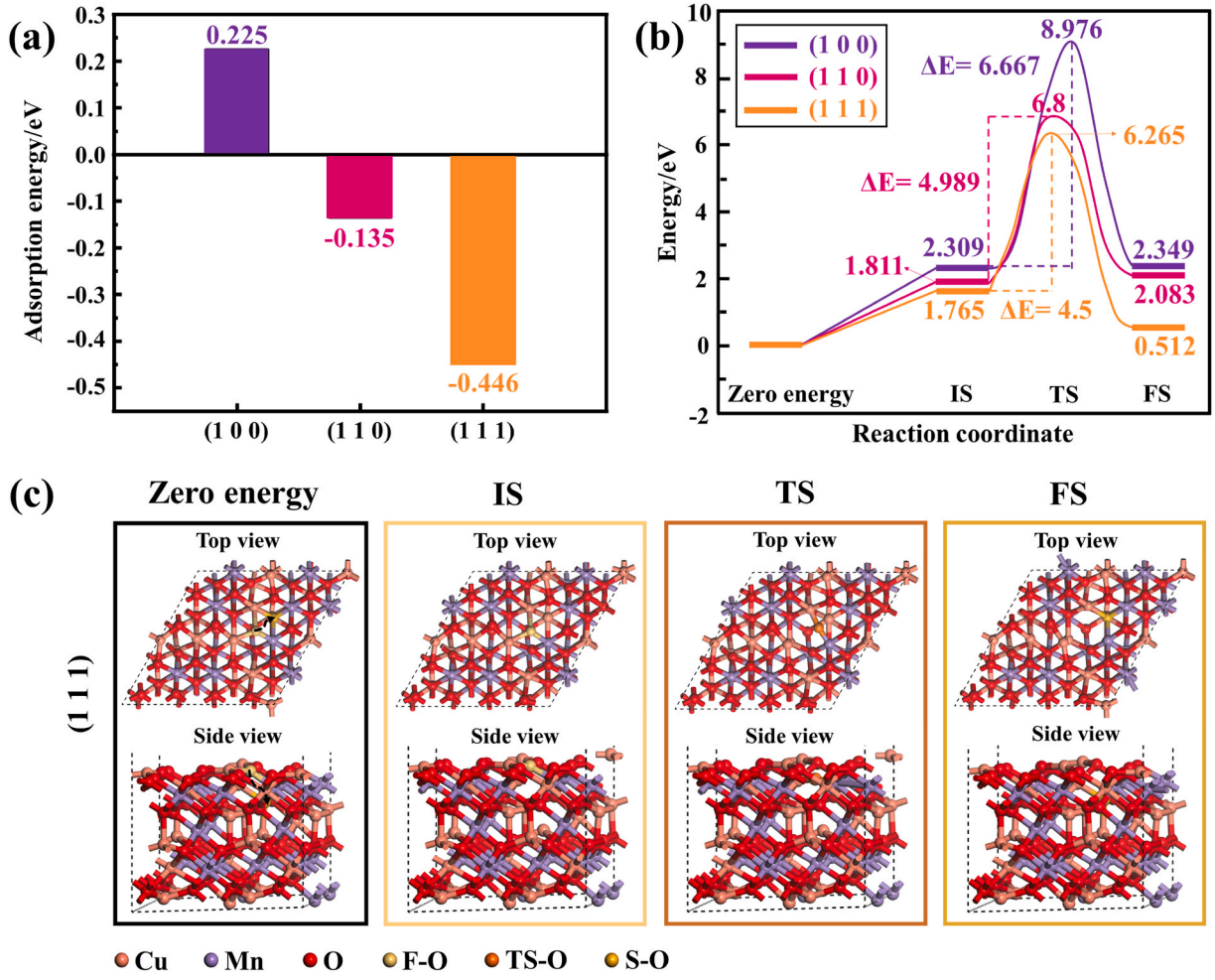

Fig. 6. DFT calculations results of directional oxygen ion diffusion. (a) Adsorption energies of O^{2-} on (100), (110) and (111) surfaces. (b) Oxygen vacancy formation energies $E(V_O)$ and diffusion energy barriers ΔE on different surfaces. (c) O diffusion pathway on (111) surface of $Cu_{1.5}Mn_{1.5}O_4$.

calculation proved that (111) surface was the optimal transport path of oxygen ions, resulting in directional voids that provide active sites for surface reactions and improve oxygen ion diffusion. Combined with experiments and calculations, we revealed the relationship between morphology changes and ion diffusion during the redox of $Cu_{1.5}Mn_{1.5}O_4$, clarified the optimal directional transport mechanism of oxygen ions, and analyzed their impact on performance improvement. This work provides an idea for the development and optimization of high-performance thermochemical energy storage materials. Through appropriate element doping, ion diffusion rate difference and optimal transport of oxygen ions can be generated, thereby creating directional voids to improve redox activity.

CRediT authorship contribution statement

Jiali Deng: Writing – original draft, Software, Methodology, Investigation, Conceptualization. **Changdong Gu:** Writing – review & editing, Validation. **Haoran Xu:** Writing – review & editing, Visualization. **Gang Xiao:** Supervision, Resources, Project administration, Funding acquisition.

Declaration of competing interest

The authors declare that they have no known competing financial interests or personal relationships that could have appeared to influence the work reported in this paper.

Data availability

Data will be made available on request.

Acknowledgments

This work was supported by the Zhejiang Science Foundation for Distinguished Young Scholars (LR20E060001), the National Natural Science Foundation of China (52176207), and the Fundamental Research Funds for the Central Universities (2022ZFJH04).

Appendix A. Supplementary data

Supplementary data to this article can be found online at https://doi.org/10.1016/j.solmat.2023.112474.

References

[1] I. Khamlich, K. Zeng, G. Flamant, J. Baeyens, C. Zou, J. Li, X. Yang, X. He, Q. Liu, H. Yang, Q. Yang, H. Chen, Technical and economic assessment of thermal energy storage in concentrated solar power plants within a spot electricity market, Renewable Sustainable Energy Rev. 139 (2021), 110583, https://doi.org/10.1016/j.rser.2020.110583.

[2] P. Del Río, C. Peñasco, P. Mir-Artigues, An overview of drivers and barriers to concentrated solar power in the European Union, Renewable Sustainable Energy Rev. 81 (2018) 1019–1029, https://doi.org/10.1016/j.rser.2017.06.038.

[3] U. Pelay, C. Azzaro-Pantel, Y. Fan, L. Luo, Life cycle assessment of thermochemical energy storage integration concepts for a concentrating solar power plant, Environ. Prog. Sustain. Energy 39 (2020), e13388, https://doi.org/10.1002/ep.13388.

[4] X. Peng, M. Yao, T.W. Root, C.T. Maravelias, Design and analysis of concentrating solar power plants with fixed-bed reactors for thermochemical energy storage, Appl. Energy 262 (2020), 114543, https://doi.org/10.1016/j.apenergy.2020.114543.

[5] X. Han, L. Wang, H. Ling, Z. Ge, X. Lin, X. Dai, H. Chen, Critical review of thermochemical energy storage systems based on cobalt, manganese, and copper oxides, Renewable Sustainable Energy Rev. 158 (2022), 112076, https://doi.org/10.1016/j.rser.2022.112076.

[6] A. Solé, I. Martorell, L.F. Cabeza, State of the art on gas-solid thermochemical energy storage systems and reactors for building applications, Renewable Sustainable Energy Rev. 47 (2015) 386–398, https://doi.org/10.1016/j.rser.2015.03.077.

[7] L. André, S. Abanades, G. Flamant, Screening of thermochemical systems based on solid-gas reversible reactions for high temperature solar thermal energy storage, Renewable Sustainable Energy Rev. 64 (2016) 703–715, https://doi.org/10.1016/j.rser.2016.06.043.

[8] L. Zeng, Z. Cheng, J.A. Fan, L.S. Fan, J. Gong, Metal oxide redox chemistry for chemical looping processes, Nat. Rev. Chem 2 (2018) 349–364, https://doi.org/10.1038/s41570-018-0046-2.

[9] A.J. Carrillo, J. González-Aguilar, M. Romero, J.M. Coronado, Solar energy on demand: a review on high temperature thermochemical heat storage systems and materials, Chem. Rev. 119 (2019) 4777–4816, https://doi.org/10.1021/acs.chemrev.8b00315.

[10] T. Block, M. Schmücker, Metal oxides for thermochemical energy storage: a comparison of several metal oxide systems, Sol. Energy 126 (2016) 195–207, https://doi.org/10.1016/j.solener.2015.12.032.

[11] M. Neises, S. Tescari, L. de Oliveira, M. Roeb, C. Sattler, B. Wong, Solar-heated rotary kiln for thermochemical energy storage, Sol. Energy 86 (2012) 3040–3048, https://doi.org/10.1016/j.solener.2012.07.012.

[12] A.P. Muroyama, A.J. Schrader, P.G. Loutzenhiser, Solar electricity via an Air Brayton cycle with an integrated two-step thermochemical cycle for heat storage based on Co3O4/CoO redox reactions II: kinetic analyses, Sol. Energy 122 (2015) 409–418, https://doi.org/10.1016/j.solener.2015.08.038.

[13] G. Karagiannakis, C. Pagkoura, A. Zygogianni, S. Lorentzou, A.G. Konstandopoulos, Monolithic ceramic redox materials for thermochemical heat storage applications in CSP plants, Energy Proc. 49 (2014) 820–829, https://doi.org/10.1016/j.egypro.2014.03.089.

[14] L. André, S. Abanades, L. Cassayre, Mixed metal oxide systems applied to thermochemical storage of solar energy: benefits of secondary metal addition in Co and Mn oxides and contribution of thermodynamics, Appl. Sci. 8 (2018) 2618, https://doi.org/10.3390/app8122618.

[15] C. Agrafiotis, M. Roeb, C. Sattler, Exploitation of thermochemical cycles based on solid oxide redox systems for thermochemical storage of solar heat. Part 4: screening of oxides for use in cascaded thermochemical storage concepts, Sol. Energy 139 (2016) 695–710, https://doi.org/10.1016/j.solener.2016.04.034.

[16] S. Setoodeh Jahromy, F. Birkelbach, C. Jordan, C. Huber, M. Harasek, A. Werner, F. Winter, Impact of partial pressure, conversion, and temperature on the oxidation reaction kinetics of Cu2O to CuO in thermochemical energy storage, Energies 12 (2019) 508, https://doi.org/10.3390/en12030508.

[17] M. Silakhori, M. Jafarian, M. Arjomandi, G.J. Nathan, Thermogravimetric analysis of Cu, Mn, Co, and Pb oxides for thermochemical energy storage, J. Energy Storage 23 (2019) 138–147, https://doi.org/10.1016/j.est.2019.03.008.

[18] D. Yilmaz, E. Darwish, H. Leion, Investigation of the combined Mn-Si oxide system for thermochemical energy storage applications, J. Energy Storage 28 (2020), 101180, https://doi.org/10.1016/j.est.2019.101180.

[19] A.J. Carrillo, P. Pizarro, J.M. Coronado, Assessing Cr incorporation in Mn2O3/Mn3O4 redox materials for thermochemical heat storage applications, J. Energy Storage 33 (2021), 102028, https://doi.org/10.1016/j.est.2020.102028.

[20] D. Xiang, C. Gu, H. Xu, G. Xiao, Self-assembled structure evolution of Mn-Fe oxides for high temperature thermochemical energy storage, Small 17 (2021), 2101524, https://doi.org/10.1002/smll.202101524.

[21] M. Deutsch, F. Horvath, C. Knoll, D. Lager, C. Gierl-Mayer, P. Weinberger, F. Winter, High-temperature energy storage: kinetic investigations of the CuO/Cu2O reaction cycle, Energy Fuels 31 (2017) 2324–2334, https://doi.org/10.1021/acs.energyfuels.6b02343.

[22] J. Fan, Y. Zhang, Y. Yang, J. Hao, Y. Wang, A. Qian, Performance of thermochemical energy storage for spinel CuMn2O4 material, J. Energy Storage 41 (2021), 102881, https://doi.org/10.1016/j.est.2021.102881.

[23] D. Xiang, C. Gu, H. Xu, J. Deng, P. Zhu, G. Xiao, Al-modified CuO/Cu2O for high-temperature thermochemical energy storage: from reaction performance to modification mechanism, ACS Appl. Mater. Interfaces 13 (2021) 57274–57284, https://doi.org/10.1021/acsami.1c17592.

[24] A.J. Carrillo, D.P. Serrano, P. Pizarro, J.M. Coronado, Thermochemical heat storage based on the Mn 2 O 3/Mn 3 O 4 redox couple: influence of the initial particle size on the morphological evolution and cyclability, J. Mater. Chem. A. 2 (2014) 19435–19443, https://doi.org/10.1039/C4TA03409K.

[25] J. Deng, C. Gu, H. Xu, G. Xiao, MgCr2O4-Modified CuO/Cu2O for high-temperature thermochemical energy storage with high redox activity and sintering resistance, ACS Appl. Mater. Interfaces 14 (2022) 43151–43162, https://doi.org/10.1021/acsami.2c09519.

[26] L. Liu, Z. Zhou, C. Wang, J. Xu, H. Xia, G. Chang, X. Liu, M. Xu, Superior thermochemical energy storage performance of the Co3O4/CoO redox couple with a cubic micro-nanostructure, J. Energy Storage 43 (2021), 103167, https://doi.org/10.1016/j.est.2021.103167.

[27] N.W. Hlongwa, D. Sastre, E. Iwuoha, A.J. Carrillo, C. Ikpo, D.P. Serrano, P. Pizarro, J.M. Coronado, Exploring the thermochemical heat storage capacity of AMn2O4 (A= Li or Cu) spinels, Solid State Ionics 320 (2018) 316–324, https://doi.org/10.1016/j.ssi.2018.03.019.

[28] X. Chen, M. Kubota, S. Yamashita, H. Kita, Exploring Cu-based spinel/delafossite couples for thermochemical energy storage at medium-high temperature, ACS Appl. Energy Mater. 4 (2021) 7242–7249, https://doi.org/10.1021/acsaem.1c01352.

[29] S. Plimpton, Fast parallel algorithms for short-range molecular dynamics, J. Comput. Phys. 117 (1995) 1–19, https://doi.org/10.1006/jcph.1995.1039.

[30] H. Zhang, B. Chen, J.F. Banfield, The size dependence of the surface free energy of titania nanocrystals, Phys. Chem. Chem. Phys. 11 (2009) 2553–2558, https://doi.org/10.1039/B819623K.

[31] G. Kresse, J. Furthmüller, Efficient iterative schemes for ab initio total-energy calculations using a plane-wave basis set, Phys. Rev. B 54 (1996), 11169, https://doi.org/10.1103/PhysRevB.54.11169.

[32] P.E. Blöchl, Projector augmented-wave method, Phys. Rev. B 50 (1994), 17953, https://doi.org/10.1103/PhysRevB.50.17953.

[33] J.P. Perdew, K. Burke, M. Ernzerhof, Generalized gradient approximation made simple, Phys. Rev. Lett. 77 (1996) 3865, https://doi.org/10.1103/PhysRevLett.77.3865.
[34] S.L. Dudarev, G.A. Botton, S.Y. Savrasov, C.J. Humphreys, A.P. Sutton, Electron-energy-loss spectra and the structural stability of nickel oxide: an LSDA+ U study, Phys. Rev. B 57 (1998) 1505, https://doi.org/10.1103/PhysRevB.57.1505.
[35] Y. Yang, J. Liu, Z. Wang, Z. Zhang, J. Ding, Y. Yu, Nature of active sites and an oxygen-assisted reaction mechanism for mercury capture by spinel-type CuMn2O4 sorbents, Energy Fuels 33 (2019) 8920–8926, https://doi.org/10.1021/acs.energyfuels.9b01696.
[36] G. Henkelman, B.P. Uberuaga, H. Jónsson, A climbing image nudged elastic band method for finding saddle points and minimum energy paths, J. Chem. Phys. 113 (2000) 9901–9904, https://doi.org/10.1063/1.1329672.
[37] R.E. Vandenberghe, G.G. Robbrecht, V.A.M. Brabers, On the stability of the cubic spinel structure in the system Cu Mn O, Mater. Res. Bull. 8 (1973) 571–579, https://doi.org/10.1016/0025-5408(73)90134-7.
[38] S. Sundar, G. Venkatachalam, S.J. Kwon, Biosynthesis of copper oxide (CuO) nanowires and their use for the electrochemical sensing of dopamine, Nanomaterials 8 (2018) 823, https://doi.org/10.3390/nano8100823.
[39] X. Yu, S. Tong, M. Ge, J. Zuo, Removal of fluoride from drinking water by cellulose@ hydroxyapatite nanocomposites, Carbohydr. Polym. 92 (2013) 269–275, https://doi.org/10.1016/j.carbpol.2012.09.045.
[40] M. Konsolakis, S.A. Carabineiro, P.B. Tavares, J.L. Figueiredo, Redox properties and VOC oxidation activity of Cu catalysts supported on Ce1- xSmxOδ mixed oxides, J. Hazard Mater. 261 (2013) 512–521, https://doi.org/10.1016/j.jhazmat.2013.08.016.
[41] R.E. Vandenberghe, G.G. Robbrect, V.A.M. Brabers, Structure and ionic configuration of oxidic copper-manganese spinels (CuxMn3-xO4), Phys. Status Solidi A 34 (1976) 583–592, https://doi.org/10.1002/pssa.2210340221.
[42] E. Ríos, S. Abarca, P. Daccarett, H.N. Cong, D. Martel, J.F. Marco, J.R. Gancedo, J. L. Gautier, Electrocatalysis of oxygen reduction on CuxMn3-xO4 (1.0≤ x≤ 1.4) spinel particles/polypyrrole composite electrodes, Int. J. Hydrogen Energy 33 (2008) 4945–4954, https://doi.org/10.1016/j.ijhydene.2008.06.030.
[43] D. Zhang, L. Zhang, L. Shi, C. Fang, H. Li, R. Gao, L. Huang, J. Zhang, In situ supported MnOx-CeOx on carbon nanotubes for the low-temperature selective catalytic reduction of NO with NH3, Nanoscale 5 (2013) 1127–1136, https://doi.org/10.1039/C2NR33006G.
[44] J. Xiao, X. Chen, P.V. Sushko, M.L. Sushko, L. Kovarik, J. Feng, Z. Deng, J. Zheng, G.L. Graff, Z. Nie, D. Choi, J. Liu, J.G. Zhang, M.S. Whittingham, High-performance LiNi0. 5Mn1. 5O4 spinel controlled by Mn3+ concentration and site disorder, Adv. Mater. 24 (2012) 2109–2116, https://doi.org/10.1002/adma.201104767.
[45] Y. Tong, L. Song, S. Ning, S. Ouyang, J. Ye, Photocarriers-enhanced photothermocatalysis of water-gas shift reaction under H2-rich and low-temperature condition over CeO2/Cu1. 5Mn1. 5O4 catalyst, Appl. Catal., B 298 (2021), 120551, https://doi.org/10.1016/j.apcatb.2021.120551.
[46] J.P. Jacobs, A. Maltha, J.G. Reintjes, J. Drimal, V. Ponec, H.H. Brongersma, The surface of catalytically active spinels, J. Catal. 147 (1994) 294–300, https://doi.org/10.1006/jcat.1994.1140.
[47] W. Yang, Y. Peng, Y. Wang, Y. Wang, H. Liu, Z.A. Su, W. Yang, J. Chen, W. Si, J. Li, Controllable redox-induced in-situ growth of MnO2 over Mn2O3 for toluene oxidation: active heterostructure interfaces, Appl. Catal., B 278 (2020), 119279, https://doi.org/10.1016/j.apcatb.2020.119279.
[48] Z. Zhang, J. Yu, J. Zhang, Q. Ge, H. Xu, F. Dallmann, R. Dittmeyer, J. Sun, Tailored metastable Ce-Zr oxides with highly distorted lattice oxygen for accelerating redox cycles, Chem. Sci. 9 (2018) 3386–3394, https://doi.org/10.1039/C8SC00729B.
[49] T. Sugimoto, General kinetics of Ostwald ripening of precipitates, J. Colloid Interface Sci. 63 (1978) 16–26, https://doi.org/10.1016/0021-9797(78)90030-9.
[50] L. Bahrig, S.G. Hickey, A. Eychmüller, Mesocrystalline materials and the involvement of oriented attachment-a review, CrystEngComm 16 (2014) 9408–9424, https://doi.org/10.1039/C4CE00882K.
[51] H.J. Fan, U. Gösele, M. Zacharias, Formation of nanotubes and hollow nanoparticles based on Kirkendall and diffusion processes: a review, Small 3 (2007) 1660–1671, https://doi.org/10.1002/smll.200700382.
[52] C. Chen, H. Hao, J. Cui, C. Yu, Y. Tang, M. Cao, Z. Yao, B. Wan, H. Liu, The role of diffusion behavior on the formation and evolution of the core-shell structure in BaTiO3-based ceramics, J. Am. Ceram. Soc. 103 (2020) 304–314, https://doi.org/10.1111/jace.16735.
[53] Z. Li, General rate equation theory for gas-solid reaction kinetics and its application to CaO carbonation, Chem. Eng. Sci. 227 (2020), 115902, https://doi.org/10.1016/j.ces.2020.115902.